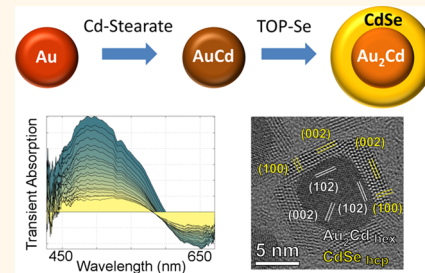


Plasmon Dynamics in Colloidal Au_2Cd Alloy–CdSe Core/Shell Nanocrystals

Pablo Guardia, Kseniya Korobchevskaya, Alberto Casu, Alessandro Genovese, Liberato Manna,* and Alberto Comin*

Department of Nanochemistry, Istituto Italiano di Tecnologia, Via Morego, 30, 16163 Genova, Italy

ABSTRACT Metal–semiconductor nanocrystal heterostructures are model systems for understanding the interplay between the localized surface plasmon resonances in the metal domain and the relaxation of the excited carriers in the semiconductor domain. Here we report the synthesis of colloidal Au_2Cd (core)/CdSe (shell) nanocrystal heterostructures, which were characterized extensively with several structural and optical techniques, including time-resolved fluorescence and broad-band transient absorption spectroscopy (both below and above the CdSe band gap). The dynamics of the transient plasmon peak was dominated by the relaxation of hot carriers in the metal core, its spectral shape was independent of the pump wavelength, and the bleaching lifetime was about half a picosecond, comparable with the value found in the AuCd seeds used for the synthesis.



KEYWORDS: colloidal nanocrystal heterostructures · plasmonic materials · plasmon bleaching dynamics · charge transfer · fluorescence quenching · metal–semiconductor nanojunctions

The most remarkable properties of colloidal nanocrystals (NCs) arise from effects such as the confinement of the electromagnetic field (localized plasmonic resonances) and/or of the charge carriers (e.g., tunable band gap).¹ Various studies have shown that the realization, within a single NC, of a nanojunction with different materials, for example a metal and a semiconductor, can lead to additional interesting physical properties, thanks to the enhancement of the electric field associated with plasmonic resonances.^{2–6} Often, however, in these “NC heterostructures” the original properties of each individual domain are masked or even modified substantially by the presence of defects at the interface(s) between the various domains and/or to interparticle charge transfer processes.^{7,8} These effects can, for example, quench the fluorescence of the semiconductor domain and, in general, alter its optical properties.^{9–12} It is well-known, for example, that when a metal NC is brought in contact with a semiconductor NC, the plasmon resonance of the metal domain is broadened due to dephasing at the interface¹³ and the fluorescence quantum efficiency of the semiconductor domain is quenched by fast charge transfer.² It is worth noting that, even in the

absence of a common interface, dipole energy transfer can contribute to quenching of the fluorescence, as shown by Kanemitsu *et al.* in closely packed arrays of Au and CdSe NCs¹⁰ and by Shevchenko *et al.* in binary Au/CdSe superlattices.¹⁴

One typical example of metal–semiconductor heterostructures is represented by Au/CdSe core/shell NCs.¹⁴ These NCs were successfully employed by Ouyang and collaborators to demonstrate ultrafast spin control by optical Stark effect.¹⁵ Similar structures have been investigated in the context of photocatalysis⁸ and to tune electrochromism and electroactivity in conducting polymers.¹⁶ Au/CdSe NCs are known to have a very weak fluorescence quantum yield: most likely, CdSe excitons dissociate because the electrons migrate to the Au domain, where they relax nonradiatively.¹⁶ This hypothesis was supported by the observation of electron–hole separation in Au/CdSe dumbbells.^{2,17} Several groups were also able to remove the positive charge from the CdSe domain in these dumbbells by adding a “hole scavenger” to the solution and retaining the extra negative charge in the Au domain for extended periods of time.^{18,19} Mid-band-gap defect states in the CdSe domain might also provide an additional

* Address correspondence to alberto.comin@iit.it, liberato.manna@iit.it.

Received for review August 17, 2012 and accepted January 7, 2013.

Published online January 08, 2013
10.1021/nn303764k

© 2013 American Chemical Society

nonradiative decay channel, which could contribute to quench the fluorescence.^{20–22} Interface defects could also trap some of the carriers, an effect that is expected to be more relevant in a core/shell type of geometry, where the contact area between the Au and the CdSe domains is proportionally much more extended than in a Au/CdSe dumbbell.

Furthermore, to date, only a few synthetic routes for the colloidal synthesis of intermetallic (*i.e.*, alloy) NCs have been published,^{23–25} even though the properties of these intermetallic NCs have recently been the subject of intensive study.^{26,27} In this context, we report in the present work colloidal heterostructures made of a core of Au₂Cd alloy surrounded by a shell of CdSe, synthesized *via* a one-pot approach developed by us. The concept we exploited is to start from gold NCs as seeds, which were converted to AuCd alloy NCs as an intermediate step. Then, as soon as a Se precursor was injected in the solution containing the AuCd NCs, this triggered the formation of a CdSe shell. One peculiarity of our synthesis method is that the Cd atoms employed for the formation of the shell appear to be supplied by the AuCd alloy NCs, with either minor or no contribution at all from residual Cd species present in solution. This assumption is supported by the fact that, upon CdSe shell growth, the composition of the core varied from AuCd to Au₂Cd, then the shell growth stopped spontaneously. Therefore, both the initial AuCd core synthesis (starting from Au NCs and evolving to AuCd NCs) and the following shell growth are self-limited by the formation of Au–Cd alloy NCs with two compositions that are particularly stable also in the bulk, namely Au₂Cd and AuCd. The AuCd NCs were therefore acting as a reservoir of Cd atoms.

The advancements brought by our synthesis approach, with respect to previously reported methods,^{28–32} include the following: (a) if the synthesis parameters are carefully chosen, the formation of byproducts, such as CdSe NCs that were usually observed in previously reported cases, is reduced (in many cases, there is no side formation of CdSe);^{28,29} (b) it yields a more symmetric core/shell structure when compared to the dumbbell-like and dimer structures that were observed in previous works;²⁹ (c) the formation of AuCd alloy NCs, as the first step toward the formation of core/shell NCs, appears to minimize the formation of aggregates of core NCs; (d) in our method, we could prepare core/shell NCs with various core sizes.

We also note that, to date, there are very few transient absorption studies on metal (or alloy) core/semiconductor (shell) NCs.^{15,33} In an early report on a system (Au/CdS) similar to ours, it was found that the recovery dynamics of the core/shell NCs was slowed down, on the picosecond time scale, with respect to the bare Au particles.³³ However, the limited time resolution prevented the authors to probe the electron–phonon time scale. Since the spectral features of the

individual Au₂Cd and CdSe domains in our core/shell NCs overlap in the visible range, in order to better understand the hot electrons' relaxation dynamics of these systems, we recorded transient absorption spectra by pumping either below (800 nm) or above the CdSe band gap (400 nm). We obtained similar spectral shape and lifetime for the plasmon peak in both cases, which indicates that most of the photons were absorbed by the Au₂Cd core. By fitting the decay of the transient absorption signal at the plasmon peak position for different pump power levels, we extracted a low-power limit of half a picosecond for the hot electrons' relaxation lifetime. Almost the same relaxation time was found for the core/shell NCs and for the AuCd NC seeds used for their synthesis. This observation indicates that in the Au₂Cd/CdSe core/shell NCs the relaxation of hot charge carriers is determined mainly by their interaction with the bulk phonons, while surface modes seem to play a minor role.

RESULTS AND DISCUSSION

Synthesis and Characterization of AuCd Alloy NCs. The first step in the synthesis of the core/shell NC reported in this work was the preparation of AuCd alloy NCs. This began from Au NC seeds, which were mixed together with oleylamine, octadecene and stearic acid as stabilizers and CdO as cadmium precursor and heated.³⁰ The addition of CdO was critical: in its absence, all of the Au NCs were unstable and aggregated as soon as the temperature reached 230 °C. Instead, in the presence of CdO, most of the NCs remained stable in solution, even at temperatures higher than 280 °C, although a small fraction still precipitated in the form of aggregates. These aggregates, which did not appear to be involved in the following shell growth, were mainly formed by Au₂Cd NCs.³⁰ It is worthy to underline that AuCd alloy NCs exhibited always a broader size distribution than the one of the starting Au seeds, caused by the high synthesis temperature, which induced strong ripening.

As soon as the temperature of this solution was increased to a critical threshold, optical absorption spectra of aliquots taken from it and dispersed in toluene indicated that the plasmon peak of the particles began shifting to the blue with respect to that of the initial Au NCs.³⁰ This shift reflected a change in the dielectric function of the initial metal NCs, most likely due to the formation of an alloy of Au with Cd.³¹ The temperature at which this process was operative scaled with the size of the initial Au NCs and ranged from 180 to 240 °C. For example, for Au seeds of 9 nm diameter, a variation in the optical spectra occurred already at 180 °C, while for bigger Au seeds, higher temperatures were required. When the plasmon reached 450 nm, the alloying process was completed, as confirmed by X-ray powder diffraction (XRD) analysis

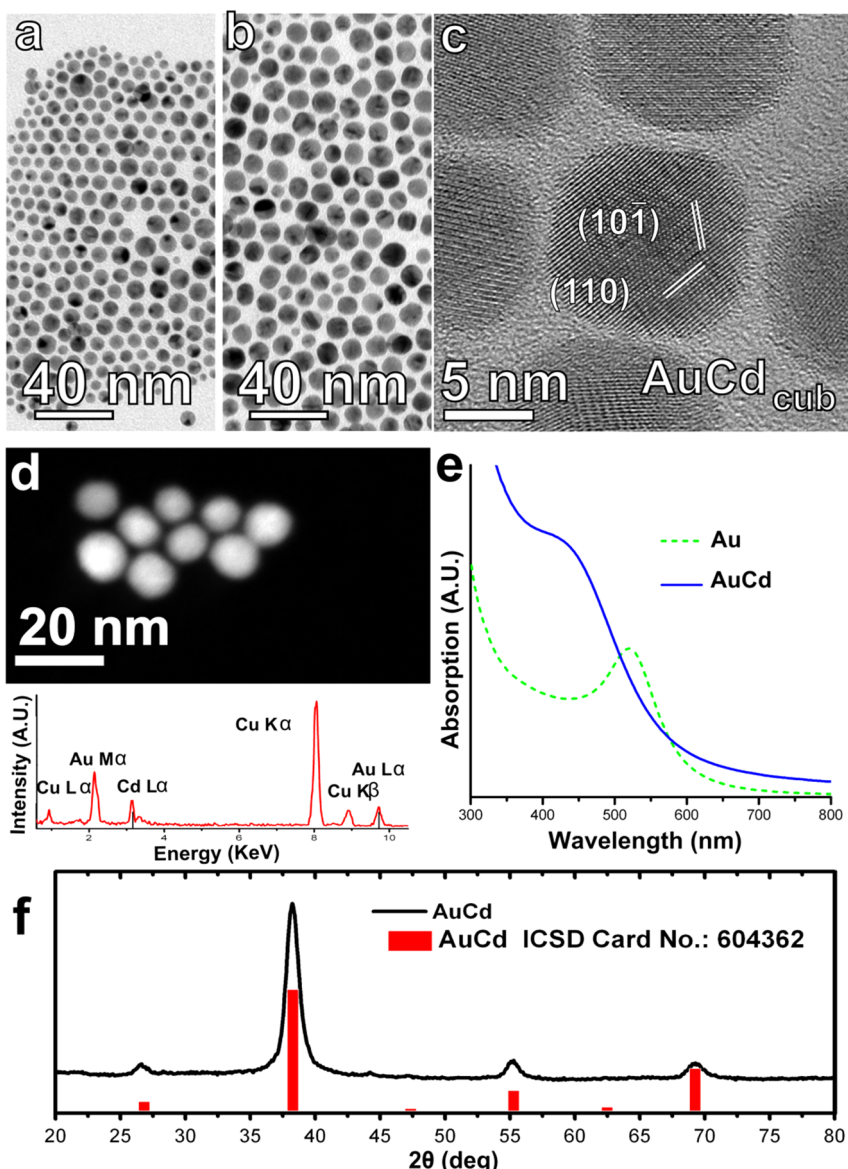


Figure 1. Survey TEM images of Au (a) and AuCd alloy (b) NCs. (c) HRTEM image of a single AuCd NC showing the typical lattice planes (110) and (10-1) with d -spacing of 2.35 Å. (d) HAADF STEM image of AuCd NCs (above) and the corresponding EDX spectrum (below) where the Cd L α and Au L α peaks are clearly recognizable. The Cu peaks come from the background signal due to the copper TEM grid. The chemical composition is consistent with an atom ratio of 1:0.94 Au/Cd. (e) Static absorption spectra of initial Au NCs (green) and resulting AuCd alloy NCs (blue). (f) XRD pattern of a cleaned sample of AuCd alloy NCs (from which aggregates had been separated), along with the positions and intensities of bulk AuCd (ICSD Card No. 604362). The broadening of the peaks is due to the small size of the NCs.

(Figure 1e,f). As a standard protocol, in all syntheses, the solution was heated at 280 °C and kept at this temperature during which the evolution in the optical spectra was completed. At this point, once the plasmon reached 450 nm, either the solution was cooled and the NCs were isolated and analyzed or a selenium precursor solution was injected at 280 °C in order to grow a CdSe shell (this second step will be discussed later). In both cases, the samples were separated from the insoluble aggregates prior to any analysis.

In the following discussion, we will focus on the alloy NCs prepared starting from the 9 nm Au seeds. The reader can refer to the Supporting Information for

additional details concerning the synthesis of alloy NCs of other diameters. The structural characterization of the resulting NCs was performed *via* high-resolution transmission electron microscopy (HRTEM) imaging and is reported in Figure 1. The measured lattice parameters and crystal direction relationship were consistent with the cubic AuCd phase where the Au/Cd atomic ratio is 1:1. Chemical analysis of these NCs, carried out with energy-dispersive X-ray spectroscopy performed in scanning TEM mode (STEM-EDX), yielded quantification characterized by an atom ratio of 1:0.94 Au/Cd using the Au and Cd L α lines, coherently with the stoichiometry of the cubic AuCd phase³⁴ (Figure 1d,

bottom panel). The size analysis was performed *via* high-angle annular dark-field STEM (HAADF STEM) imaging and yielded an average diameter of 10 ± 2 nm. A representative HAADF STEM image of AuCd alloy NCs is shown in Figure 1d (top panel). We also performed XRD analysis, with the resulting XRD pattern exhibiting the peaks of the AuCd phase (Figure 1f).^{35,36}

In the bulk, both 1:1 and 2:1 Au/Cd ratios represent thermodynamically stable phase compositions for this alloy.^{35,36} However, in our case, only the AuCd NCs did not aggregate in solution, while the Au₂Cd NCs precipitated out. Most likely, for the latter NCs, the surface passivation by the surfactants present in the reaction environment was not effective enough to stabilize them in solution.

Synthesis and Characterization of Au₂Cd/CdSe Core/Shell NCs. As anticipated in the previous section, in order to synthesize Au₂Cd/CdSe NCs, as soon as the formation of AuCd alloy NCs was completed in the mixture heated at 280 °C, a solution of selenium dissolved in trioctylphosphine (TOP) was injected in the reaction flask (see the Methods section for more details), after which the temperature was allowed to recover to 280 °C. Upon injection, optical absorption spectra of aliquots taken from the solution evidenced a red shift of the plasmon peak (Figure 2d), which suggested a CdSe shell growth on top of the alloy NCs. This was confirmed by TEM (Figure 2a). In the following, we will focus on one sample of Au₂Cd/CdSe NCs, synthesized using 9 nm Au seeds and under synthesis conditions that yielded Au₂Cd/CdSe NCs with an overall size of 15 ± 2.4 (10 ± 2 nm for the core and 2.5 ± 1.8 nm the shell, respectively). Additional data for syntheses performed using other seed sizes or under different reaction conditions are reported in the Supporting Information.

Crystal structure characterization *via* HRTEM of the core/shell NCs indicated, for the cores, lattice parameters that were consistent with a hexagonal Au₂Cd phase (ICSD Card 659134) and for the shell a CdSe wurtzite phase (ICSD Card 659134) (Figure 2b). Moreover, the two lattices (that of the Au₂Cd core and that of the CdSe shell) were epitaxially related: as clearly shown in Figure 2b, the hexagonal Au₂Cd core domains were delimited by peripheral {102} facets, which formed angles of 93° and 87° with each other. These Au₂Cd{102} facets also constituted the epitaxial interfaces for the heterogeneous growth of hexagonal CdSe shells, which maintained the same angular relationship of the original Au₂Cd{102} facets. For this reason, the Au₂Cd/CdSe heterostructures had a quasi-cubic morphology when observed along the Au₂Cd-[010] zone axis, as shown in Figure 2b.³⁰ A STEM-EDX line profile, performed across a group of core/shell NCs, revealed the Au, Cd and Se elemental distribution (Figure 2c), while STEM-EDX chemical quantification yielded atomic ratios of Au/Cd equal to 2:0.9 for the cores and Cd/Se equal to 1:1 for the shells.³³ XRD

analysis confirmed the presence of both Au₂Cd and CdSe phases (Figure 2e).

We tried to tune the shell size of the Au₂Cd/CdSe NCs by varying the synthesis conditions. However, any attempt to achieve larger shell thicknesses, for example by increasing the amount of Se/TOP solution injected and/or the amount of CdO used (in the first step), ended up in the side nucleation of separate CdSe NCs (see Figures S3 and S4 of the Supporting Information). On the other hand, a comparison between several samples differing in the size of the starting AuCd seeds did not evidence a clear difference in the shell thickness of the final Au₂Cd/CdSe NCs as the difference within the experimental data was within the experimental error. However, most likely, the Cd atoms employed for the shell growth were those supplied from the initial AuCd alloy NCs, with either minor contribution or no contribution at all from residual Cd species present in solution. This was further supported by the variation of the Cd stoichiometry in the NC cores during shell growth, which decreased from AuCd to Au₂Cd, after which the shell growth self-arrested.³⁶ The volume variation of a single AuCd NC when 50% of Cd atoms were extracted to form a Au₂Cd NC is 37%. This variation produces a size decrease of about 11% which is comparable with the size dispersion.³³ The exact mechanism governing this process is unclear: the diffusions of Cd atoms toward the outer regions of the NCs could be activated either by the formation of a Se-rich layer in the peripheral regions of the NCs and/or by a diffusion of Se species a few nanometers inside the AuCd NCs.

In the core/shell NCs, the optical absorption spectra exhibited a red shift of the plasmon peak with respect to that of the AuCd seeds, as highlighted above. There are two main causes for such a red shift. One effect is related to the different dielectric environment felt by the NC cores after a CdSe shell is grown on them: initially, the cores, contained in an aliquot extracted from the reaction flask, were diluted in toluene (refractive index equal to 1.5). Upon shell growth, the cores were embedded in a material with much higher refractive index (between 2.6 and 2.7 for the bulk hexagonal phase of CdSe).³⁷ This change in dielectric environment would already account for a red shift of around 50 nm in the plasmonic response. The other effect is clearly related to the change in stoichiometry of the core, from AuCd to Au₂Cd, which influences its dielectric function and brings it closer to that of gold.

Disentangling these two contributions to the optical response, in the present case, is not trivial, first of all because there is no literature data on how the dielectric function of a Au–Cd alloy depends on its relative composition. As a first approximation, it would be tempting to neglect interband transitions and to assume that the stoichiometry of the Au–Cd alloy NCs is what mainly affects the plasmon resonance

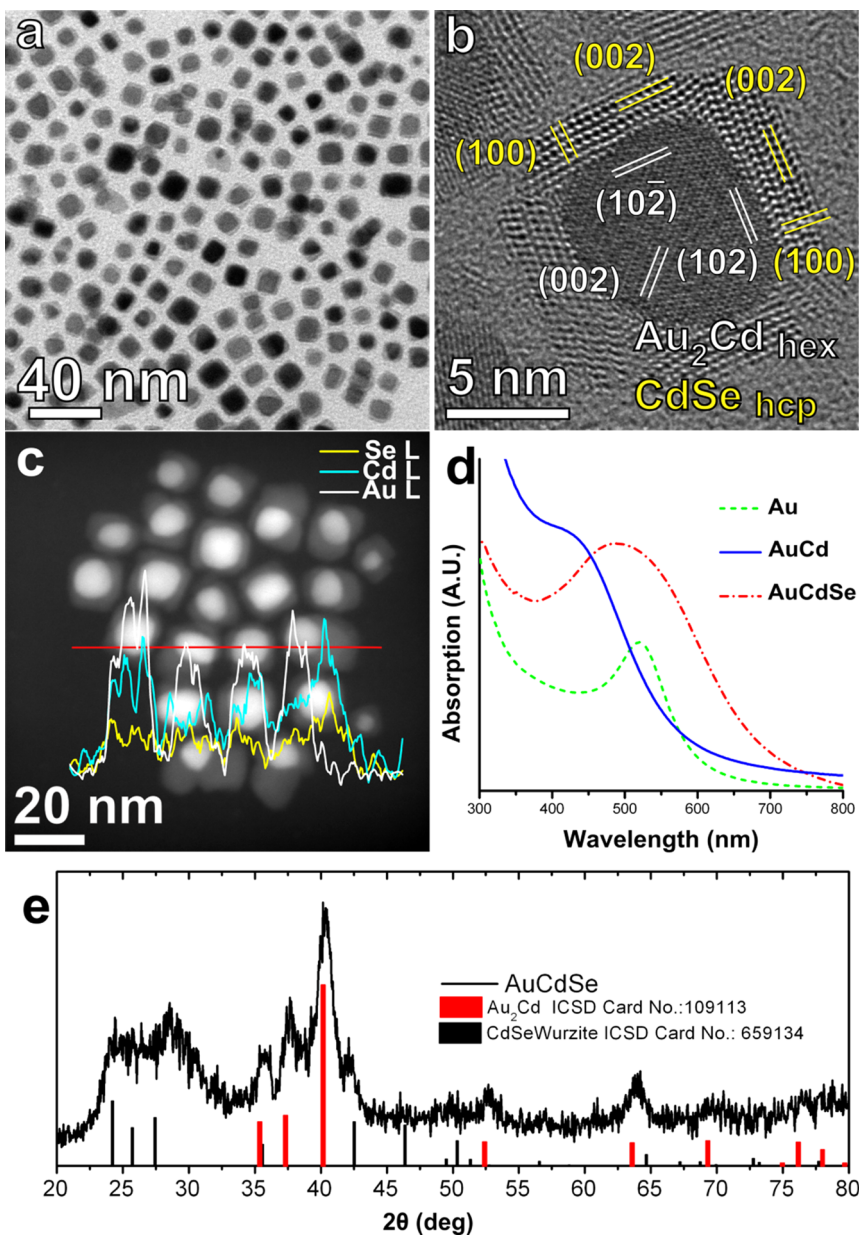


Figure 2. (a) Survey TEM image of $\text{Au}_2\text{Cd}/\text{CdSe}$ core/shell NCs. (b) HRTEM image of a single $\text{Au}_2\text{Cd}/\text{CdSe}$ core/shell NC exhibiting the characteristic (102) and (002) lattice planes of hexagonal Au_2Cd , in the core, with measured d -spacings of 1.74 and 2.4 Å, respectively, and the (100) and (002) lattice planes of hexagonal CdSe , in the shell, with measured d -spacings of 3.72 and 3.5 Å, respectively. (c) Survey HAADF STEM image of a group of $\text{Au}_2\text{Cd}/\text{CdSe}$ core/shell NCs. Both CdSe shells (faint contrast) and Au_2Cd cores (bright contrast) are visible. EDX line profile (red line) exhibits Au , Cd , and Se distribution across the cores and the shells along the horizontal direction. (d) Static absorption spectra of Au (green), AuCd (blue), and $\text{Au}_2\text{Cd}/\text{CdSe}$ (red) samples. (e) XRD pattern of the $\text{Au}_2\text{Cd}/\text{CdSe}$ sample, along with the bulk positions and intensities of Au_2Cd (ICSD Card No. 109113) and CdSe (wurtzite, ICSD Card No. 659134).

frequency, *via* a change in the free electron density. If, for simplicity, we assume that each Au atom contributes with one free electron and each Cd atom contributes with two electrons, it would be straightforward to estimate the free electron density, given the known values for the lattice constant of the specific alloy under study. Then, the Drude model and the Mie theory could be used to calculate the expected variation of the surface plasmon resonance, in function of the stoichiometry of the core. In the case of $\text{Au}_2\text{Cd}/\text{CdSe}$ core/shell NCs, however, the surface plasmon

resonance is in a frequency range where interband transitions are dominant.³¹ A more accurate model would be needed, which should describe how the dielectric function of a $\text{Au}-\text{Cd}$ alloy NC is affected by the stoichiometry.

It is nonetheless worthy of note that, differently from some previous reports on Au/CdSe and $\text{Au}_2\text{Cd}/\text{CdSe}$ core/shell NCs, in which the Au plasmon was almost suppressed by the presence of the CdSe shell,^{29,38} our samples preserved a pronounced plasmonic peak. As it can be noticed from Figure 2d, the plasmon peak of the $\text{Au}_2\text{Cd}/\text{CdSe}$ core/shell NCs was

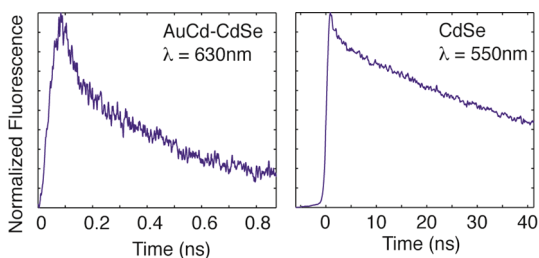


Figure 3. Time-resolved fluorescence signals of $\text{Au}_2\text{Cd}/\text{CdSe}$ NCs recorded at 630 nm (left panel) and of CdSe NCs recorded at 550 nm (right panel).

asymmetric. Since the CdSe absorbance was basically negligible for wavelengths above its band gap (590 nm), the relatively large absorbance of the core/shell samples above 600 nm could originate from the presence of contributions from mid-band-gap defect states in the red side of the spectrum.

Time-Resolved Optical Characterization. Figure 3 shows the fluorescence time decays of core/shell NCs ($\lambda = 630$ nm, right panel) and of a control sample of CdSe NCs ($\lambda = 550$ nm, left panel, note the compressed time scale). In the figure, the long raise time of the fluorescence signal was due to the time jitter of the streak camera. First, the fluorescence from the CdSe shell in the $\text{Au}_2\text{Cd}/\text{CdSe}$ heterostructures was quenched. This was expected because the metal–semiconductor junction provides a nonradiative decay channel for the carriers that are photoexcited in the CdSe shell. The core/shell signal could be fitted with two exponential decays: 40 ± 3 and 480 ± 30 ps. The time constants of the reference CdSe sample were longer: 1200 ± 100 and 59 ± 4 ns. As was mentioned in the introduction, according to previous published works, the main cause of the fluorescence quenching in $\text{Au}_2\text{Cd}/\text{CdSe}$ NCs should be electron transfer from CdSe to the metal domain.³⁹ We verified this by comparing the lifetime of the core/shell NCs with the lifetime of CdSe NCs, with the same volume as the CdSe shell in the core/shell NCs (Figure 3).

Transient absorption spectra of the core/shell NCs contain information on both Au_2Cd and CdSe domains, as well as on the interaction between them. If the two domains are spatially separated, the dipole–dipole energy transfer is the dominant interaction. If they are in contact, as in the present case, charge transfer and delocalization of free carriers can occur. In particular, the relaxation of the quantum confinement in Au/CdSe heterostructures has been proposed to explain the bleaching of both excitonic and plasmonic features in these systems.¹³ To interpret transient absorption spectra in the present core/shell NCs, it is useful to compare measurements performed with a pump wavelength both below (800 nm) and above (400 nm) the band gap of CdSe. A below-band-gap pump excites only the core of the NCs and an above-band-gap one excites both core and shell simultaneously. Figure 4 reports

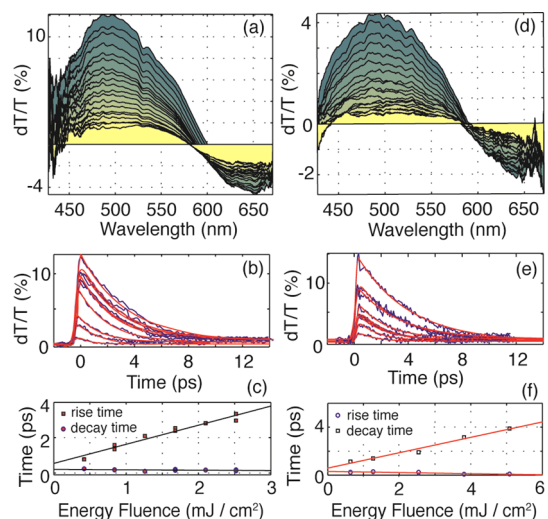


Figure 4. Transient absorption spectra of core/shell NCs measured with pump wavelengths corresponding to (a) 400 nm and (d) 800 nm. The various color shades refer to different time delays. Slices of transient spectra at the peak wavelength are reported in (b) and (e), together with fit lines. (c,d) Pump power dependence of the rise and decay times, obtained by fitting the data shown in (b) and (e).

the transient spectra with pump at 400 nm (inset a) and 800 nm (inset d). The curves at different time delays are stacked one on the top of the other and are color-coded for ease of comparison. The overall shape of the transient spectra did not depend on the pump wavelength, meaning that the main contribution to the signal originated from the Au_2Cd core. In particular, both the central peak position (495 nm) and the width of the transient plasmon peak did not depend on the pump wavelength (whether 400 or 800 nm). It can be noticed that in both cases the positive peak was initially asymmetric, then it shifted to the red and became more symmetric. In general, this can be caused by an intrinsic effect or by sample inhomogeneity. In the first case, one possibility is that the observed shift of the transient absorption peak between 490 and 530 nm is caused by energy transfer between the hot electrons photoexcited in the Au_2Cd core and either interface states or excitons generated in the CdSe shell.

However, it can be expected that sample inhomogeneity contributes at least partially to the overall shape of the transient plasmonic peak. Indeed, particles of different core size or in which the core is nested differently inside the CdSe shell can have different plasmon peak positions and different plasmon bleaching relaxation times. We note, however, that, by statistical analysis of TEM images, we did not detect partially coated nor unreacted AuCd seeds in the sample solution. If uncoated particles were present in the solution, they would have caused in addition a time-dependent change in the plasmon peak profile. Indeed, coated and uncoated particles have not only different plasmon frequencies but also different relaxation times because of their different heat conductivity.

The plasmon bleaching decay times were estimated by fitting the transient absorption signals at the plasmon peak (see Figure 4b–e) and repeating the procedure for different power levels (this is necessary because the specific heat of free electrons is proportional to their temperature; see ref 40). In order to fit the data, we used a pulse function obtained as convolution of a Gaussian and a double exponential.⁴¹ Figure 4c–f reports the fitted time constants as a function of the pump power. It can be seen that the decay times are comparable for 400 and 800 nm pump wavelengths. This is different from what was previously observed in similar systems. Kobayashi *et al.* observed, for example, a wavelength-dependent transient absorption signal in Au/PbS core/shell NCs. However, in their case, the contribution from the shell was more significant than in our case.⁴² In theory, for the 400 nm pump, one could expect a transient blue shift of the plasmon resonance due to the transfer of photoexcited electrons from the CdSe shell to the Au₂Cd core.⁴³ Probably, this effect is not observable in our system, where most photons are absorbed by the Au₂Cd core (see Figure 2d) and the number of carriers that are photo-generated in the CdSe is very small. An optically thicker CdSe shell could contribute more photocarriers and lead, after charge transfer, to an observable plasmon shift.⁴⁴

By extrapolating the fitted decay times to zero pump power, it was possible to estimate a low-power limit lifetime for the plasmon decay.⁴⁰ We obtained 0.6 ± 0.1 ps for the measurements at 400 nm and 0.6 ± 0.1 ps for those at 800 nm. These values are similar to what we found for the AuCd seeds and are consistent with previously published values for Au NCs.^{45–47} However, a precise comparison is not trivial. In these systems, the wave function of the core electrons can extend inside the shell region,¹³ and the electrons that are photo-excited in the core could also relax by exchanging energy with CdSe electronic excitations. Therefore, we argue that, in these systems, the plasmonic bleaching lifetime can be more correctly understood as a lower limit for the electron–phonon coupling in the Au₂Cd core. The electron–phonon relaxation time is similar in NCs and in the bulk, except for very small NCs, where the spill-out effect reduces the measured lifetime.⁴⁵

In metal NCs, in addition to the standard electron–phonon coupling found in bulk,⁴⁵ hot electrons relax *via* breathing acoustic phonon modes,⁴⁸ as can be evidenced by single-particle measurements.⁴⁰ Since

the shell and the core in our system have different elastic constants, the frequencies of the breathing modes are expected to be different for NC seeds and for core/shell NCs. It is therefore peculiar that the electron–phonon coupling time seems to be unaffected by the shell. In similar experiments by our group, performed on Au/Fe_xO_y core/shell NCs, we found a significant difference of the electron–phonon coupling in the core/shell sample with respect to that of Au NCs, the core/shell NCs relaxation being twice faster than for the Au NCs.⁴¹ We therefore conclude that the hot relaxation dynamics in Au₂Cd/CdSe core/shell NCs is dominated by the coupling with bulk phonons, with the interface playing a minor role, at least on the picosecond time scale.

CONCLUSIONS

We have reported the synthesis of core/shell NCs, consisting of a Au₂Cd core and a CdSe shell. These were obtained starting from AuCd alloy seeds, upon their reaction with a Se precursor, which triggered the extraction of part of the Cd atoms from the AuCd core, and led to the formation of a CdSe shell. We extensively characterized the seeds and the core/shell NCs and measured the plasmon bleaching dynamics *via* broadband transient absorption spectroscopy. The transient plasmonic peak of the core/shell NCs was initially asymmetric, then evolved in time and became more symmetric and red-shifted after a few picoseconds. The plasmon bleaching lifetime was about 0.6 ps, regardless of whether the excitation was below or above the CdSe band gap. This opens up the possibility of tuning the optical properties of the shell without affecting the plasmonic response of the core and represents an important advancement toward the realization of devices combining plasmonic and semiconductor nanostructures.

The use of gold nanorods as seeds in the synthesis of Au₂Cd/CdSe core shell structures, though challenging, would be of interest for a better understanding of these core/shell systems since their longitudinal plasmon frequency can be tuned below the threshold for the onset of the interband transition of Au₂Cd. Unfortunately, preliminary experiments in our lab showed that the synthesis of AuCd nanorods (NR), starting from a Au NR, is so far hindered by the fast aggregation of the Au NR at the temperatures required for the alloying process. Work is in progress in our laboratories to try to overcome these issues.

METHODS

Synthesis of AuCd NC Alloy and Au₂Cd(Core)/CdSe(Shell). AuCd NCs and Au₂Cd(core)/CdSe(shell) NCs were sequentially synthesized by using gold NCs as initial/starting seeds. The latter were prepared according to literature procedures.³⁰ In a typical

synthesis of 10 ± 2 nm AuCd alloy NCs, in a three-neck flask, 1.5 mL of 1-octadecene, 50 mg of stearic acid and 5 mg of cadmium oxide were degassed and heated in order to form cadmium stearate. After cooling the solution to 65 °C, 6 mL of oleylamine and 1.5 mL of a solution of 9 ± 2 nm Au NCs in hexane (concentration of gold atoms was equal to 9.13 mM)

and the hexane was evaporated for 120 min at 65 °C under vacuum. The solution was finally heated to 280 °C, and aliquots were collected from time to time; they were diluted in toluene, and the optical absorption spectra were recorded. Once the solution reached 280 °C and the plasmon reached 450 nm, the flask was cooled to room temperature as fast as possible and the NCs were precipitated by addition of methanol. After washing, particles were dispersed in toluene and centrifuged for 5 min at 1000 rpm in order to remove aggregates. The final solution was used for further characterization.

In order to synthesize $\text{Au}_2\text{Cd}(\text{core})/\text{CdSe}(\text{shell})$ NCs, the same procedure described above was repeated but was not stopped at the formation of the AuCd alloy NCs. Instead, as soon as this was completed in the mixture heated at 280 °C, 300 μL of trioctylphosphine/Se solution (32 g/L of Se, obtained by dissolving Se powder in trioctylphosphine) was injected in the flask, and the resulting mixture was allowed to react for 5 min. As for the synthesis of AuCd alloy NCs, particles were collected by centrifugation and aggregates were discarded by centrifugation.³⁰

Structural and Morphological Characterization. The morphological characterization of the NCs was carried out *via* transmission electron microscopy (TEM) using a JEOL JEM 1011 microscope working at an accelerating voltage of 100 keV. High-resolution TEM (HRTEM) and high-angle annular dark-field (HAADF) in scanning TEM mode (STEM) measurements were performed with a JEOL JEM-2200FS microscope equipped with a field emission gun working at an accelerating voltage of 200 kV and a CEOS spherical aberration corrector of the objective lens allowing to reach a spatial resolution of 0.9 Å. The chemical composition of the NCs was determined by energy-dispersive X-ray spectroscopy (EDX) analysis performed in STEM mode with a JED-2300 Si(Li) detector, using an electron probe of 0.7 nm and the Cliff-Lorimer method for the elemental quantifications.

XRD measurements were performed on a Rigaku SmartLab X-ray diffractometer operating at 40 kV and 150 mA. The diffractometer was equipped with Cu source and a Gobel mirror in order to have a parallel beam, and it was used in $2\theta/\Omega$ scan geometry for the acquisition of the data. Specimens for XRD measurement were prepared in the glovebox by dropping a concentrated NC solution onto a zero background silicon substrate.

Optical Characterization. Steady-state optical absorption spectra were recorded in toluene using a Varian Cary 5000 UV-vis-NIR spectrophotometer, with 1 cm quartz cells. Transient absorption measurements were performed with a femtosecond pump-probe setup (Coherent Micro and Legend: central wavelength 800 nm, bandwidth 30 nm, pulse duration 60 fs, repetition rate 1 kHz) as previously described.⁴¹ Spot sizes were 1 mm for the pump and 0.5 mm for the probe. Part of the laser output was frequency doubled and used as pump, and part was focused into a 3 mm sapphire plate to produce the supercontinuum probe beam. All samples were loaded in 1 mm quartz cells, and the group velocity dispersion was numerically compensated for the probe beam. Time-resolved fluorescence measurements were performed using a streak camera (Hamamatsu C5680), optically synchronized with the laser and coupled with a monochromator. The sample was stored in 1 mm quartz cell and excited by a 400 nm beam near normal incidence. The fluorescence was collected with a 10 cm lens at normal incidence from the same side as the excitation and refocused with an identical lens to the entrance slit of the monochromator.

Conflict of Interest: The authors declare no competing financial interest.

Acknowledgment. This work was financially supported in part by the FP7 starting ERC Grant NANOARCH (Contract No. 240111).

Supporting Information Available: Additional details on synthesis. This material is available free of charge *via* the Internet at <http://pubs.acs.org>.

REFERENCES AND NOTES

1. Cortie, M. B.; McDonagh, A. M. Synthesis and Optical Properties of Hybrid and Alloy Plasmonic Nanoparticles. *Chem. Rev.* **2011**, *111*, 3713–3735.
2. Costi, R.; Saunders, A. E.; Banin, U. Colloidal Hybrid Nanostructures: A New Type of Functional Materials. *Angew. Chem., Int. Ed.* **2010**, *49*, 4878–4897.
3. Govorov, A. O.; Bryant, G. W.; Zhang, W.; Skeini, T.; Lee, J.; Kotov, N. A.; Slocik, J. M.; Naik, R. R. Exciton–Plasmon Interaction and Hybrid Excitons in Semiconductor–Metal Nanoparticle Assemblies. *Nano Lett.* **2006**, *6*, 984–994.
4. Achermann, M. Exciton–Plasmon Interactions in Metal–Semiconductor Nanostructures. *J. Phys. Chem. Lett.* **2010**, *1*, 2837–2843.
5. Mokari, T.; Rothenberg, E.; Popov, I.; Costi, R.; Banin, U. Selective Growth of Metal Tips onto Semiconductor Quantum Rods and Tetrapods. *Science* **2004**, *304*, 1787–1790.
6. Lin, H. Y.; Chen, Y. F.; Wu, J. G.; Wang, D. I.; Chen, C. C. Carrier Transfer Induced Photoluminescence Change in Metal–Semiconductor Core–Shell Nanostructures. *Appl. Phys. Lett.* **2006**, *88*, 161911–161913.
7. Hirakawa, T.; Kamat, P. V. Charge Separation and Catalytic Activity of $\text{Ag}@\text{TiO}_2$ Core–Shell Composite Clusters under UV–Irradiation. *J. Am. Chem. Soc.* **2005**, *127*, 3928–3934.
8. Kim, Y.; Park, K. Y.; Jang, D. M.; Song, Y. M.; Kim, H. S.; Cho, Y. J.; Myung, Y.; Park, J. Synthesis of $\text{Au}–\text{Cu}_2\text{S}$ Core–Shell Nanocrystals and Their Photocatalytic and Electrocatalytic Activity. *J. Phys. Chem. C* **2010**, *114*, 22141–22146.
9. Shaviv, E.; Banin, U. Synergistic Effects on Second Harmonic Generation of Hybrid $\text{CdSe}–\text{Au}$ Nanoparticles. *ACS Nano* **2010**, *4*, 1529–1538.
10. Kanemitsu, Y.; Matsuda, K. Energy Transfer between Excitons and Plasmons in Semiconductor–Metal Hybrid Nanostructures. *J. Lumin.* **2011**, *131*, 510–514.
11. He, S.; Zhang, H.; Delikanli, S.; Qin, Y.; Swihart, M. T.; Zeng, H. Bifunctional Magneto-Optical $\text{FePt}–\text{CdS}$ Hybrid Nanoparticles. *J. Phys. Chem. C* **2009**, *113*, 87–90.
12. Chen, W.-T.; Yang, T.-T.; Hsu, Y.-J. $\text{Au}–\text{CdS}$ Core–Shell Nanocrystals with Controllable Shell Thickness and Photo-induced Charge Separation Property. *Chem. Mater.* **2008**, *20*, 7204–7206.
13. Khon, E.; Mereshchenko, A.; Tarnovsky, A. N.; Acharya, K.; Klinkova, A.; Hewa-Kasakarage, N. N.; Nemitz, I.; Zamkov, M. Suppression of the Plasmon Resonance in $\text{Au}–\text{CdS}$ Colloidal Nanocomposites. *Nano Lett.* **2011**, *11*, 1792–1799.
14. Shevchenko, E. V.; Ringler, M.; Schwemer, A.; Talapin, D. V.; Klar, T. A.; Rogach, A. L.; Feldmann, J.; Alivisatos, A. P. Self-Assembled Binary Superlattices of CdSe and Au Nanocrystals and Their Fluorescence Properties. *J. Am. Chem. Soc.* **2008**, *130*, 3274–3275.
15. Zhang, J.; Tang, Y.; Lee, K.; Ouyang, M. Tailoring Light–Matter–Spin Interactions in Colloidal Hetero-nanostructures. *Nature* **2010**, *466*, 91–95.
16. Bhandari, S.; Deepa, M.; Sharma, S. N.; Joshi, A. G.; Srivastava, A. K.; Kant, R. Charge Transport and Electrochromism in Novel Nanocomposite Films of Poly(3,4-ethylenedioxythiophene)– Au Nanoparticles– CdSe Quantum Dots. *J. Phys. Chem. C* **2010**, *114*, 14606–14613.
17. Costi, R.; Cohen, G.; Salant, A.; Rabani, E.; Banin, U. Electrostatic Force Microscopy Study of Single $\text{Au}–\text{CdSe}$ Hybrid Nanodumbbells: Evidence for Light-Induced Charge Separation. *Nano Lett.* **2009**, *9*, 2031–2039.
18. Gao, B.; Lin, Y.; Wei, S.; Zeng, J.; Liao, Y.; Chen, L.; Goldfeld, D.; Wang, X.; Luo, Y.; Dong, Z.; et al. Charge Transfer and Retention in Directly Coupled $\text{Au}–\text{CdSe}$ Nanohybrids. *Nano Res.* **2012**, *5*, 88–98.
19. Costi, R.; Saunders, A. E.; Elmaleh, E.; Salant, A.; Banin, U. Visible Light-Induced Charge Retention and Photocatalysis with Hybrid $\text{CdSe}–\text{Au}$ Nanodumbbells. *Nano Lett.* **2008**, *8*, 637–641.
20. Yan, J.-Y.; Zhang, W.; Duan, S.; Zhao, X.-G.; Govorov, A. Optical Properties of Coupled Metal–Semiconductor and Metal–Molecule Nanocrystal Complexes: Role of Multipole Effects. *Phys. Rev. B* **2008**, *77*, 165301.
21. Pons, T.; Medintz, I. L.; Sapsford, K. E.; Higashiyama, S.; Grimes, A. F.; English, D. S.; Mattoussi, H. On the Quenching of Semiconductor Quantum Dot Photoluminescence by Proximal Gold Nanoparticles. *Nano Lett.* **2007**, *7*, 3157–3164.

22. Manjavacas, A.; García de Abajo, F.; Nordlander, P. Quantum Plexcitonics: Strongly Interacting Plasmons and Excitons. *Nano Lett.* **2011**, *11*, 2318–2323.

23. Chen, W.; Yu, R.; Li, L.; Wang, A.; Peng, Q.; Li, Y. A Seed-Based Diffusion Route to Monodisperse Intermetallic CuAu Nanocrystals. *Angew. Chem., Int. Ed.* **2010**, *122*, 2979–2983.

24. Lu, Y.-C.; Xu, Z.; Gasteiger, H. A.; Chen, S.; Hamad-Schifferli, K.; Shao-Horn, Y. Platinum–Gold Nanoparticles: A Highly Active Bifunctional Electrocatalyst for Rechargeable Lithium–Air Batteries. *J. Am. Chem. Soc.* **2010**, *132*, 12170–12171.

25. Wanjala, B. N.; Luo, J.; Fang, B.; Mott, D.; Zhong, C.-J. Gold–Platinum Nanoparticles: Alloying and Phase Segregation. *J. Mater. Chem.* **2011**, *21*, 4012–4020.

26. Ding, X.; Zou, Y.; Jiang, J. Au–Cu₂S Heterodimer Formation via Oxidation of AuCu Alloy Nanoparticles and *In Situ* Formed Copper Thiolate. *J. Mater. Chem.* **2012**, *22*, 23169–23174.

27. Zeng, J.; Huang, J.; Liu, C.; Wu, C. H.; Lin, Y.; Wang, X.; Zhang, S.; Hou, J.; Xia, Y. Gold-Based Hybrid Nanocrystals through Heterogeneous Nucleation and Growth. *Adv. Mater.* **2010**, *22*, 1936–1940.

28. Lee, J.-S.; Shevchenko, E. V.; Talapin, D. V. Au–PbS Core–Shell Nanocrystals: Plasmonic Absorption Enhancement and Electrical Doping via Intra-particle Charge Transfer. *J. Am. Chem. Soc.* **2008**, *130*, 9673–9675.

29. Lu, W.; Wang, B.; Zeng, J.; Wang, X.; Zhang, S.; Hou, J. G. Synthesis of Core/Shell Nanoparticles of Au/CdSe via Au–Cd Bimetallic Precursor. *Langmuir* **2005**, *21*, 3684–3687.

30. For additional details, see the Supporting Information.

31. Maier, S. A. *Plasmonics: Fundamentals and Applications*; Springer: New York, 2007.

32. AbouZeid, K. M.; Mohamed, M. B.; El-Shall, M. S. Hybrid Au–CdSe and Ag–CdSe Nanoflowers and Core–Shell Nanocrystals via One-Pot Heterogeneous Nucleation and Growth. *Small* **2011**, *7*, 3299–3307.

33. Kamat, P. V.; Shanghavi, B. Interparticle Electron Transfer in Metal/Semiconductor Composites. Picosecond Dynamics of CdS-Capped Gold Nanoclusters. *J. Phys. Chem. B* **1997**, *101*, 7675–7679.

34. Alasafi, K. M.; Schubert, K. Kristallstruktur von AuCd.r. *J. Less-Common Met.* **1977**, *55*, 1–8.

35. Byström, A.; Almin, K. E. X-ray Investigation of Gold–Cadmium Alloys Rich in Gold. *Acta Chem. Scand.* **1947**, *1*, 76–89.

36. Rivlin, V.; Hume-Rothery, W.; Ryder, B. The Constitution and Structure of Gold–Cadmium Alloys. *Acta Metall. Mater.* **1962**, *10*, 1143–1150.

37. Schäffner, M.; Bao, X.; Penzkofer, A. Principal Optical Constants Measurement of Uniaxial Crystal CdSe in the Wavelength Region between 380 And 950 nm. *Appl. Opt.* **1992**, *31*, 4546–4552.

38. Rajasekhar Pullabhotla, V. S. R.; Revaprasadu, N. A Novel Route to Cysteine Capped Au–CdSe Hybrid Nanoparticles. *Mater. Lett.* **2009**, *63*, 2097–2099.

39. Wood, A.; Giersig, M.; Mulvaney, P. Fermi Level Equilibration in Quantum Dot–Metal Nanojunctions. *J. Phys. Chem. B* **2001**, *105*, 8810–8815.

40. Hartland, G. V. Optical Studies of Dynamics in Nobel Metal Nanostructures. *Chem. Rev.* **2011**, *111*, 3858–3887.

41. Comin, A.; Korobchevskaya, K.; George, C.; Diaspro, A.; Manna, L. Plasmon Bleaching Dynamics in Colloidal Gold–Iron Oxide Nanocrystal Heterodimers. *Nano Lett.* **2012**, *12*, 921–926.

42. Kobayashi, Y.; Nonoguchi, Y.; Wang, L.; Kawai, T.; Tamai, N. Dual Transient Bleaching of Au/PbS Hybrid Core/Shell Nanoparticles. *J. Phys. Chem. Lett.* **2012**, *3*, 1111–1116.

43. Choi, H.; Chen, W. T.; Kamat, P. V. Know Thy Nano Neighbor. Plasmonic *versus* Electron Charging Effects of Metal Nanoparticles in Dye-Sensitized Solar Cells. *ACS Nano* **2012**, *6*, 4418–4427.

44. Mongin, D.; Shaviv, E.; Maioli, P.; Crut, A.; Banin, U.; Del Fatti, N.; Vallée, F. Ultrafast Photoinduced Charge Separation in Metal–Semiconductor Nano-hybrids. *ACS Nano* **2012**, *6*, 7034–7043.

45. Arbouet, A.; Voisin, C.; Christofilos, D.; Langot, P.; Del Fatti, N.; Vallée, F.; Lermé, J.; Celep, G.; Cottancin, E.; Gaudry, M. M.; et al. Electron–Phonon Scattering in Metal Clusters. *Phys. Rev. Lett.* **2003**, *90*, 177401.

46. Voisin, C.; Christofilos, D.; Loukakos, P.; Del Fatti, N.; Vallée, F.; Lermé, J.; Gaudry, M.; Cottancin, E.; Pellarin, M.; Broyer, M. Ultrafast Electron–Electron Scattering and Energy Exchanges in Noble-Metal Nanoparticles. *Phys. Rev. B* **2004**, *69*, 195416.

47. Hodak, J.; Martini, I.; Hartland, G. V. Ultrafast Study of Electron–Phonon Coupling in Colloidal Gold Particles. *Chem. Phys. Lett.* **1998**, *284*, 135–141.

48. Voisin, C.; Del Fatti, N.; Christofilos, D.; Vallée, F. Ultrafast Electron Dynamics and Optical Nonlinearities in Metal Nanoparticles. *J. Phys. Chem. B* **2001**, *105*, 2264–2280.